JACS
JOURNAL OF THE AMERICAN CHEMICAL SOCIETY
Article
pubs.acs.org/JACS

Nonaqueous Synthesis of TiO_2 Nanocrystals Using TiF_4 to Engineer Morphology, Oxygen Vacancy Concentration, and Photocatalytic Activity

Thomas R. Gordon,[†] Matteo Cargnello,[∥] Taejong Paik,[†] Filippo Mangolini,[§] Ralph T. Weber,[⊥] Paolo Fornasiero,[∥] and Christopher B. Murray*[,†,‡]

[†]Department of Chemistry, [‡]Department of Materials Science and Engineering, [§]Department of Mechanical Engineering and Applied Mechanics, University of Pennsylvania, Philadelphia, Pennsylvania 19104, United States

[∥]Department of Chemical and Pharmaceutical Sciences, ICCOM-CNR, INSTM, Center of Excellence for Nanostructured Materials (CENMAT), University of Trieste, Trieste, Italy

[⊥]Bruker BioSpin Corporation, Billerica, Massachusetts 01821, United States

Supporting Information

ABSTRACT: Control over faceting in nanocrystals (NCs) is pivotal for many applications, but most notably when investigating catalytic reactions which occur on the surfaces of nanostructures. Anatase titanium dioxide (TiO_2) is one of the most studied photocatalysts, but the shape dependence of its activity has not yet been satisfactorily investigated and many questions still remain unanswered. We report the nonaqueous surfactant-assisted synthesis of highly uniform anatase TiO_2 NCs with tailorable morphology in the 10−100 nm size regime, prepared through a seeded growth technique. Introduction of titanium(IV) fluoride (TiF_4) preferentially exposes the {001} facet of anatase through *in situ* release of hydrofluoric acid (HF), allowing for the formation of uniform anatase NCs based on the truncated tetragonal bipyramidal geometry. A method is described to engineer the percentage of {001} and {101} facets through the choice of cosurfactant and titanium precursor. X-ray diffraction studies are performed in conjunction with simulation to determine an average NC dimension which correlates with results obtained using electron microscopy. In addition to altering the particle shape, the introduction of TiF_4 into the synthesis results in TiO_2 NCs that are blue in color and display a broad visible/NIR absorbance which peaks in the infrared ($\lambda_{max} \approx 3400$ nm). The blue color results from oxygen vacancies formed in the presence of fluorine, as indicated by electron paramagnetic resonance (EPR) and X-ray photoelectron spectroscopy (XPS) studies. The surfactants on the surface of the NCs are removed through a simple ligand exchange procedure, allowing the shape dependence of photocatalytic hydrogen evolution to be studied using monodisperse TiO_2 NCs. Preliminary experiments on the photoreforming of methanol, employed as a model sacrificial agent, on platinized samples resulted in high volumes of evolved hydrogen (up to 2.1 mmol h^{-1} g^{-1}) under simulated solar illumination. Remarkably, the data suggest that, under our experimental conditions, the {101} facets of anatase are more active than the {001}.

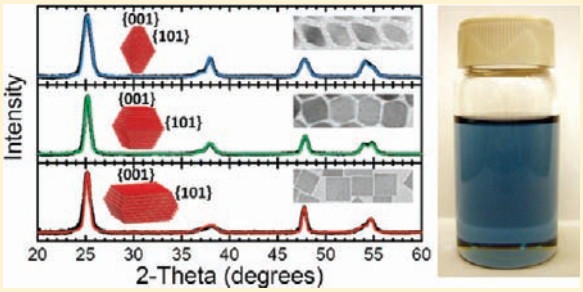

INTRODUCTION

Titanium dioxide (TiO_2) is an industrially important wide-band gap semiconductor, with an annual production of greater than one million metric tons each year in the United States alone.[1] In addition to the traditional applications of TiO_2 in the fields of coatings, ceramics, and cosmetics, nanostructuring of TiO_2 has enabled its use as an active material in sensors, electrochromics, gas-phase catalysts, fuel cells, lithium-ion batteries, photovoltaics, photoelectrochemical cells, and photocatalysts.[2,3] TiO_2 has several advantages over other inorganic materials, including earth abundance, low toxicity, chemical and thermal stability, and resistance to photocorrosion.[2−4] Three polymorphs of TiO_2 exist naturally: rutile, anatase, and brookite.[5] While rutile is the most thermodynamically stable bulk phase, anatase has been shown by numerous studies to be more photocatalytically active than rutile and is often dominant in nanocrystalline TiO_2, due to having lower surface energy than rutile.[2,5,6] Brookite is a low-temperature stable phase and is usually obtained as a mixture with the other polymorphs of TiO_2.[7] High surface area TiO_2 nanomaterials have been synthesized for many years through a variety of techniques, including sol−gel, hydrothermal, and chemical vapor deposition (CVD) methods and have immense promise in future nanoengineered materials.[2]

In the context of photocatalysis, numerous recent publications have focused on synthetically controlling the facets exposed in the anatase phase of TiO_2.[8−11] Studies of single

Received: January 25, 2012
Published: March 24, 2012

   dx.doi.org/10.1021/ja300823a | *J. Am. Chem. Soc.* 2012, 134, 6751−6761

crystalline surfaces have shown that the particular facets exposed during photocatalytic reactions dramatically influence both reaction rate and selectivity.[5,6,12,13] The most stable form of the anatase polymorph is a tetragonal bipyramidal structure in which primarily {101} facets of anatase are exposed, with a small percentage of {001} facets, as predicted by the Wulff construction.[14] Yang et al. recently demonstrated that the introduction of hydrofluoric acid (HF) during the hydrothermal synthesis of TiO_2 stabilizes the {001} facet relative to the {101} facet, allowing for the formation of truncated bipyramidal structures, in the micrometer-size range.[8] The authors also suggest, based on theoretical calculations, that the {001} facet has higher reactivity compared to the {101} facet due to having a higher concentration of low coordination Ti_{5c} centers. This has subsequently created a surge of interest regarding the relative reactivity of the various facets of anatase TiO_2 under illumination, both theoretically[15,16] and experimentally.[17−23] Currently, reports are mixed concerning which facet results in higher photocatalytic activity, possibly due to the multitude of reaction conditions investigated.[17,22,24,25] Moreover, the relative activity of the {001} and {101} facets has primarily been determined for large anatase crystallites (~0.2−5 μm in size), with very few examples reporting the photocatalytic activity of high-surface area, nanosized catalysts which are more relevant for practical applications. Obtaining uniformity in both the morphology and phase composition of TiO_2 at the nanoscale is nontrivial using traditional synthetic methods, and preferential exposure of the {001} facet of anatase often necessitates the use of concentrated HF, which is hazardous to handle.[26]

In the past two decades, nonaqueous surfactant assisted synthetic methods have revolutionized the production of highly monodisperse and shape-controlled nanocrystals (NCs) composed of a variety of materials, including catalytically relevant metals and metal oxides.[27−31] Through optimization of the synthetic parameters, these techniques provide the most precise and reproducible control over particle size and morphology, enabling the production of model systems for catalysis with near-atomic precision in size and control over faceting.[32−39] NCs produced through these methods are typically phase pure single crystals and may be activated through ligand exchange or mild oxidative treatment, requiring no high temperature annealing.[39−42] In addition, because the NCs are surfactant stabilized, they are highly soluble in nonaqueous solvents. This enables numerous preparation techniques which are not typically available for the production of traditional catalysts, including the formation of thin films through spin-coating,[43] liquid interfacial assembly,[37] and self-assembly.[32] TiO_2 NCs of rutile, anatase, and brookite phases with various morphologies have been synthesized using these techniques, but the photocatalytic activity of these materials has not been exhaustively explored.[40,41,44−52] Overall, this nonaqueous approach provides unparalleled ability to tune the shape and size of monodisperse catalytic NCs to precisely tune the surface area and exposed facets in NCs, which enables the derivation of structure−activity relationships. While the coupling of synthetic control of faceting with catalytic activity has been achieved for metallic NCs, very few studies have investigated the influence of faceting on the photocatalytic activity of NCs. In particular, to our knowledge, a detailed analysis of the morphologically dependent activity of uniform TiO_2 NCs for photocatalytic H_2 production has not been reported to date.

In this paper, we report the controlled synthesis of highly uniform TiO_2 NCs in the 10−100 nm size regime which are prepared through a seeded growth technique.[49,53,54] The titanium precursor titanium(IV) fluoride (TiF_4) releases HF *in situ*, which acts as a structure directing agent and allows for better morphological control than previously obtained in hydrothermal syntheses which require the direct handling of HF. We show that the percentage of {001} and {101} facets in the tetragonal bipyramidal anatase TiO_2 NCs can be engineered through the choice of the titanium precursor and cosurfactant. X-ray diffraction studies, in conjunction with simulation, allow for the determination of the average NC dimension in a given sample which correlates with results obtained through electron microscopy. In addition to enabling shape control, TiF_4 is observed to alter the optical properties of the NCs. UV−vis−NIR−IR optical spectroscopy, low temperature electron paramagnetic resonance (EPR) spectroscopy, and X-ray photoelectron spectroscopy (XPS) suggest that TiO_2 NCs produced in the presence of TiF_4 are oxygen deficient and that the NC surfaces are partially fluorinated. The photocatalytic activity of the platinized TiO_2 NCs is tested for the evolution of hydrogen in the presence of methanol as a model sacrificial agent. Within the series of anatase NCs, those with more {101} facets exposed are observed to have the highest activity, which is consistent with recent experimental reports.

EXPERIMENTAL SECTION

Chemicals. The following chemicals are used as received without further purification. Titanium(IV) fluoride (TiF_4, 99%), titanium(IV) chloride ($TiCl_4$, 99%), nitrosonium tetrafluoroborate ($NOBF_4$), 1-octadecene (90%) (1-ODE), 1-octadecanol (1-ODOL, 97%), *N*,*N*-dimethylformamide (DMF), toluene, hexanes, acetone, methanol, and 2-propanol are purchased from Acros Organics. Oleylamine (OLAM, 70%), oleic acid (OLAC, 90%), acetonitrile (ACN), and potassium tetrachloroplatinate(II) (K_2PtCl_4, ≥99.9%) are purchased from Sigma Aldrich.

Preparation of Stock Solutions. Stock solutions are prepared in a glovebox under a nitrogen atmosphere. The TiF_4 stock solution consists of 0.2 M TiF_4 and 1.0 M OLAC in 1-ODE. The $TiCl_4$ stock solution consists of 0.2 M $TiCl_4$ and 1.0 M OLAC in 1-ODE. The TiF_4 stock solution is stirred on a hot plate set to 80 °C to promote the dissolution of TiF_4. Once dissolved, the TiF_4 stock solution is orange-brown and the $TiCl_4$ stock solution is dark brown.

Synthesis of TiO_2 NCs. All syntheses are performed using standard Schlenk line techniques under a nitrogen atmosphere. A general procedure proceeds as follows. In a 125 mL flask, 30 mmol of cosurfactant (OLAM or 1-ODOL), 10.2 mL of 1-ODE, and 0.48 mL (1.5 mmol) of OLAC are combined and degassed at 120 °C for 1 h. For 1:1 mixtures, TiF_4 and $TiCl_4$ stock solutions are mixed at equal volume in the glovebox. After degassing the flask, 1.5 mL of the desired stock solution (or mixed stock solution) is added at 60 °C. Then, the solution is quickly heated to 290 °C and held 10 min to allow for the formation of seed crystals. An 8 mL portion of the chosen stock solution is then pumped into the flask kept at 290 °C at 0.3 mL min^{-1} using a New Era Pump Systems NE-1000 syringe pump. Afterward, the heating mantle is removed and the flask is left to cool naturally to ambient temperature. For simplicity, TiO_2 NC samples will be referred to as X-cosurfactant, where X refers to the stock solution used, i.e., F (for TiF_4), Cl (for $TiCl_4$), or M (for 1:1 mixture). Therefore, a sample synthesized with TiF_4 and 1-ODOL will be referred to as F-ODOL.

Workup. Post-synthesis, the reaction contents are first diluted with a small volume of toluene and centrifuged at 6000 rpm to separate the NCs. The NCs are then redispersed through the addition of toluene and 100 μL of OLAM with sonication. Insoluble surfactant and agglomerated particles are removed through centrifugation. A mixture of 2-propanol and methanol is added to precipitate the NCs, and

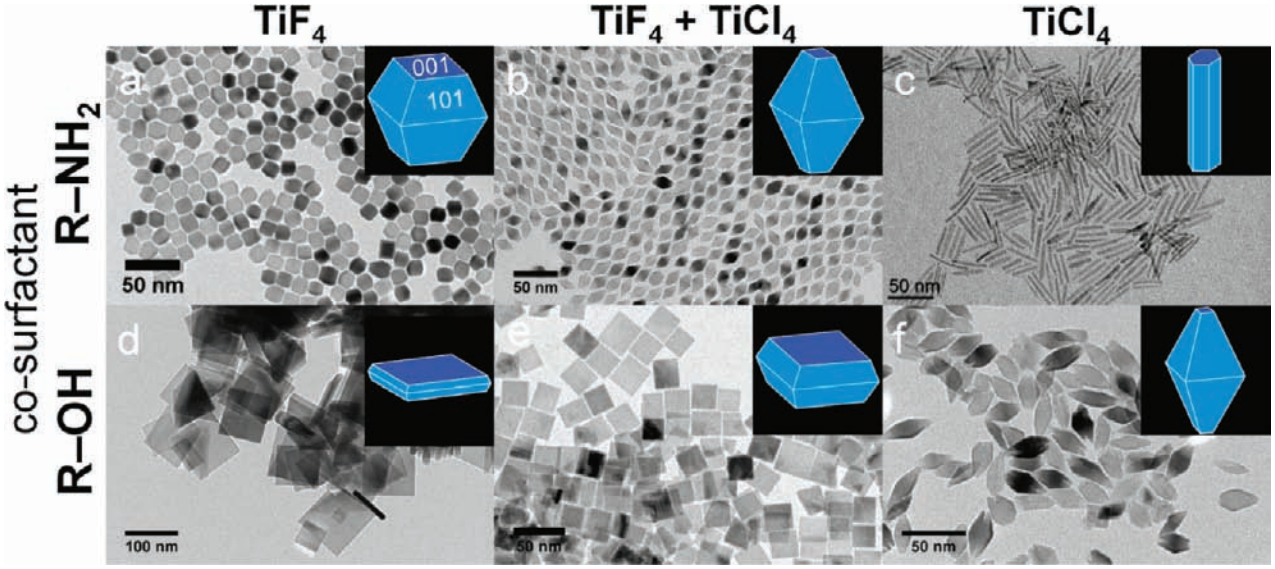

Figure 1. TEM images of TiO_2 NCs synthesized using the precursor TiF_4 (a,d), a mixed precursor of TiF_4 and $TiCl_4$ (b,e), and $TiCl_4$ (c,f). Those depicted in a–c and d–f are synthesized in the presence of OLAM and 1-ODOL, respectively.

centrifugation at 6000 rpm is used to recover the NCs. This washing process was repeated twice. NCs with dimensions less than 30 nm are subsequently highly soluble in nonpolar or low-polarity solvents including hexanes, toluene, carbon tetrachloride, tetrachloroethylene, and chloroform. Larger particles are sparingly soluble, forming stable suspensions in the same solvents.

Ligand Exchange with $NOBF_4$. In a centrifuge tube, 0.1 g of $NOBF_4$ and 10 mL of ACN are combined and sonicated, resulting in the formation of a yellow solution indicating the solublization of $NOBF_4$. A 10 mL aliquot of the $NOBF_4$ saturated ACN is added to the hexanes solution (10 mL) of NCs (50–150 mg). The NCs quickly become insoluble and are collected through centrifugation. The solid is then completely solubilized in DMF with sonication. To remove residual organics, DMF solutions are washed through the addition of a mixture of toluene and hexanes until precipitation occurs, followed by centrifugation. This process is repeated three times. After the final centrifugation, the NCs are dried in a vacuum oven at 60 °C overnight to remove residual solvent molecules. Once dry, each sample is ground in an agate mortar and pestle into a fine powder with grain dimensions below 150 μm.

NaOH Treatment of TiO_2 NCs. The removal of fluorine is performed by treating the samples with a NaOH solution according to the work of Minella et al.[55] Briefly, ~50 mg of the powder are dispersed in 5 mL of NaOH aqueous solution at pH 12 (~0.01 M) and stirred in the dark for 8 h. The powder is recovered by filtration (Millipore 0.45 μm), washed with 1 mM HCl and twice distilled water, and finally dried at 50 °C for 8 h.

Photocatalytic Activity. The photocatalytic activity of the ligand-exchanged and NaOH-treated NCs is evaluated for hydrogen production using methanol as the model sacrificial agent. Approximately 27 mg of the NCs is suspended with sonication in 80 mL of an aqueous solution of methanol (1:1 by volume, final concentration of NCs ca. 0.3 M). K_2PtCl_4 is added to obtain a final loading of platinum of 1 wt %. The suspension is irradiated using a Solar Simulator (LOT-Oriel) (see Figure S1 for lamp spectrum) equipped with a 150 W Xe lamp filtered with an atmospheric filter to reduce the fraction of UV photons. An Ar flow (15 mL min^{-1}) ensures the complete removal of air from the reactor and that the reaction products reach the detector. An external recirculation bath is used to keep the temperature of the reactor constant at 20 °C.

Gaseous products are analyzed by gas chromatography (GC) using a thermal conductivity detector (TCD) for the quantification of H_2 and CO_2 with He as the carrier. The liquid phase byproducts are analyzed by gas chromatography/mass spectrometry (GC/MS) using an HP 7890 GC equipped with a DB-225ms column (J&W) and an HP 5975C mass spectrometer.

Characterization. Transmission electron microscopy (TEM) images were recorded using a JEOL JEM1400 TEM equipped with an SC1000 ORIUS CCD camera operating at 120 kV. High-resolution TEM (HRTEM) images were recorded on a JEOL 2010F operating at 200 kV. Samples were prepared by drop-casting a dispersion of NCs in toluene or hexanes on a 300 mesh carbon-coated copper TEM grid followed by drying at 50 °C under vacuum. Scanning electron microscopy (SEM) images and energy dispersive X-ray spectroscopy (EDS) spectra were recorded on a JEOL JSM7500F equipped with an Oxford X-stream EDS detector. Samples were prepared on 150 mesh carbon-coated copper TEM grids as described above. All X-ray diffraction (XRD) patterns were recorded on a Rigaku Smartlab diffractometer equipped with a Cu K_α source. For transmission measurements (2θ scan), NCs were placed as highly concentrated toluene solutions into 1.0 mm glass capillaries. For reflection measurements (θ–2θ scan), NCs were dropcast from concentrated hexanes solutions onto glass slides. UV–vis–NIR spectra were recorded on a Varian Cary 5000 spectrometer, equipped with a Harrick praying mantis DRS accessory for diffuse reflectance spectra (DRS). For DRS, powdered samples were diluted at 2 wt % in KBr and pure KBr was used as a background. IR spectra were recorded on a Thermo-Fisher Continuμm FT-IR system in transmission mode using a Harrick demountable liquid cell. EPR spectra were collected for powder samples on a Bruker Elexys E500 spectrometer at the frequency 9.391 GHz at the Bruker Biospin Corporation. Samples for XPS analysis were dropcast from 1:10 solutions of octane/hexanes onto Si wafers and then treated in Ar plasma for 4 min using a Gatan Solarus Model 950 plasma cleaner to remove the bound surfactants. XPS analyses were carried out with a customized X-ray photoelectron spectrometer (a VG Scienta R3000 customized for elevated pressure operation). Briefly, the XP-spectrometer is equipped with a monochromatic Al K_α source (VG Scienta MX 650). The electrons emitted from the specimen are collected with an electrostatic lens, whose axis is normal to the sample surface. The acceptance angle of the input lens system is 14°. After passing the hemispherical analyzer, the photoelectrons are detected by a two-dimensional MCP/CCD detector. In the present work, the X-ray source was run at 30 mA and 12 kV, while the analyzer was operated in constant-analyzer-energy (CAE) mode. Further information about the XPS measurements and the quantitative analysis is reported in the Supporting Information. N_2 physisorption experiments were carried out on a Micromeritics ASAP

dx.doi.org/10.1021/ja300823a | J. Am. Chem. Soc. 2012, 134, 6751–6761

2020C. The samples were first degassed in vacuum at 120 °C for 19 h prior to N_2 adsorption at liquid nitrogen temperature.

X-ray Diffraction Simulation. The q-dependent powder X-ray diffraction intensity, $I(q)$, is calculated using the Debye equation as described previously:[27]

$$I(q) = I_0 \sum_m \sum_n F_m F_n \frac{\sin(qr_{mn})}{qr_{mn}}$$

where I_0 is the incident intensity, $q = 4\pi \sin\theta/\lambda$ is the scattering parameter for X-rays of wavelength λ diffracted through the angle θ, and r_{mn} is the distance between atoms m and n, with atomic form factors F_m and F_n, respectively. Atomic form factors are calculated from tabulated Cromer–Mann coefficients.[56,57] To improve calculation time, the Debye equation is discretized by binning identical distances to give the following equation:[58]

$$I(q) = \frac{I_0}{q} \sum_m \sum_n F_m F_n \frac{\rho(r_{mn})}{r_{mn}} \sin(qr_{mn})$$

where $\rho(r_{mn})$ is the multiplicity of each unique distance r_{mn} in the structure. Particle size distribution is incorporated using a probability distribution, where each final pattern is the Gaussian weighted sum of 21 or more patterns from individual NCs.

RESULTS AND DISCUSSION

Seeded Growth Synthesis of TiO_2 Nanocrystals. The synthesis of TiO_2 NCs is based on a seeded growth approach.[49] Small TiO_2 nanocrystallites (or "seeds") are first formed by combining a small quantity of titanium(IV) halide (TiX_4) dissolved in oleic acid (OLAC) with a large molar excess of the cosurfactant (oleylamine (OLAM) or 1-octadecanol (1-ODOL)) in solvent 1-octadecene (1-ODE) and quickly heating to 290 °C. After a 10 min induction period in which anatase TiO_2 seeds form (Figure S2), a stock solution of TiX_4 dissolved in OLAC/1-ODE is slowly added to the seed solution via syringe pump, enabling the progressive growth of the nanocrystalline seeds and preventing further nucleation.[49,53,54] The addition of cosurfactant OLAM or 1-ODOL is essential, as these molecules accelerate the formation of TiO_2 under nonaqueous conditions, as discussed in more detail below.

Transmission electron microscopy (TEM) images (Figure 1) show the range of morphologies achievable through the present approach, depending on the choice of cosurfactant and titanium(IV) halide (TiX_4) under otherwise identical reaction conditions. We observe dramatic differences in the morphology of the obtained NCs when using TiF_4 as the titanium precursor compared to using $TiCl_4$. In the presence of cosurfactant OLAM, TiF_4 produces highly uniform tetragonal bipyramidal anatase NCs (sample F-OLAM) which are significantly truncated perpendicular to the [001] direction (Figure 1a). In the case of $TiCl_4$, pure phase brookite nanorods (Cl-OLAM), similar to as reported previously, are produced (Figure 1c).[49] With cosurfactant 1-ODOL, TiF_4 results in anatase nanoplates (F-ODOL) with a high percentage of {001} facets (Figure 1d), while $TiCl_4$ produces tetragonal bipyramidal anatase NCs (Cl-ODOL) with primarily {101} facets (Figure 1f). The size of the NCs is observed to increase with time as more stock solution is added (Figure S3). In accordance with recent syntheses performed under aqueous conditions, we observe that the use of fluorine containing species results in the preferential exposure of the {001} facet of anatase, truncating the bipyramidal base morphology of the NCs.[8,10]

The percentage of {001} and {101} facets in the TiO_2 NCs is further controlled through use of a mixed precursor solution consisting of equimolar TiF_4 and $TiCl_4$ as the precursor for the seeded growth of TiO_2 NCs. Using cosurfactant OLAM, highly monodisperse anatase tetragonal bipyramidal NCs are formed with the mixed precursor (M-OLAM), which have a small percentage of {001} facets. The mixed precursor in combination with 1-ODOL forms nanoplates (M-ODOL) with large percentages of {001} facets, although not as high a percentage as observed with a pure TiF_4 precursor and the particle size is much reduced. Thus, the present synthetic technique provides a means to tune both the size and truncation of anatase tetragonal bipyramidal NCs by modifying the surfactants and precursors in nonaqueous solution.

Mechanism of Shape Control. We have demonstrated that the choice of both titanium precursor and cosurfactants dramatically influences the morphology of TiO_2 NCs. Through an investigation of the reaction mechanism under nonaqueous conditions, we can rationalize why these effects are observed. The first step in the synthesis is the dissolution of TiX_4 precursors in the presence of OLAC. Short chain carboxylic acids have been shown to complex with $TiCl_4$ at low temperature in nonaqueous solutions, resulting in the formation of stable mono- and polynuclear chlorotitanium carboxylate complexes and the release of HCl.[59−61] Similarly, we expect the coordination of OLAC with titanium centers upon dissolution of titanium(IV) halides (TiX_4) into solutions of OLAC/1-ODE, releasing hydrohalic acids (HX) into the solution. In the case of TiF_4, this translates to the *in situ* release of HF, which acts as a shape directing agent, providing the fluoride ions which bind selectively to the {001} facet of anatase TiO_2 and manipulate the NC shape.[8]

In the presence of cosurfactant, the halotitanium carboxylate complex decomposes due to chemical reactions with the surfactant molecules. Aminolysis of titanium carboxylate complexes is known to occur at high temperature in solutions of OLAM, OLAC, and organometallic titanium precursors, hydroxylating the titanium center (X_3Ti-OH) and producing oleyl amide as a byproduct.[47,49] The mechanism for the decomposition of the titanium complex in the presence of 1-ODOL and OLAC is more difficult to ascertain, due to the fact that multiple reaction pathways are feasible. In the absence of carboxylic acids, alcohols are known to react directly with TiX_4 to form X_3Ti-OH or titanium alkoxides (X_3Ti-OR).[62−65] In addition, the free alcohol or the formed X_3Ti-OR could react with the titanium carboxylate complex to generate X_3Ti-OH and an ester as a byproduct, as described previously.[62,64,66] We propose that a single mechanism is unlikely in the presence of 1-ODOL and OLAC. In any case, formation of X_3Ti-OH is followed by polymerization to form TiO_2 and, under nonhydrolytic conditions, the release of additional HX.

The species HF formed *in situ* is proposed to be a shape directing agent, binding selectively to the {001} facet of anatase and altering the shape of the resulting NCs. By using a mixed precursor (1:1 F/Cl), the amount of HF released is significantly reduced, and the percentage of {001} facets in the resulting NCs is decreased. Likewise, we observe significant differences in the percentage of {001} facets depending on the choice of cosurfactant. Under otherwise identical reaction conditions, NCs produced in the presence of 1-ODOL have much higher percentages of {001} facets relative to the NCs synthesized in OLAM, indicating the presence of more HF in solution. This may be rationalized by considering the expected reaction of HF with the excess OLAM in solution to produce a primary ammonium fluoride salt ($RNH_3^+ F^-$). Through this reaction, the amine sequesters the HF generated, reducing the amount of

fluorine available to bind to the {001} facet of anatase. In this way, the cosurfactant may be used to influence the particle shape. In addition to preferentially exposing the {001} facet, fluoride precursors have been shown to stabilize the anatase phase, preventing a phase transformation to rutile.[67,68] The stabilizing effect of fluorine on the anatase phase may explain why there is no phase transformation to the brookite phase in F-OLAM, as observed with Cl-OLAM.

Structural Characterization by X-ray Diffraction. Precise knowledge of the particular facets exposed in a catalytic material is pivotal in formulating structure−activity relationships. In the case of photocatalysis on anatase TiO_2, it is well-known that the percentages of {001} and {101} facets have a dramatic influence on the photocatalytic activity.[69] In the literature, the dimensions of the anatase crystals (from which the percentages of the facets are extracted) are determined through the analysis of electron microscopy images. While electron microscopy is an invaluable tool for morphological determination, image analysis to extract statistically significant shape and size information is time-consuming and is inevitably prone to bias and error. In addition, the accurate quantification of the dimension of a crystal becomes increasingly difficult with decreasing particle size. This is especially true when measuring the thickness of nanoplates and nanosheets which necessitates that the long axis of the crystal aligns nearly perpendicular to the substrate. Electron microscopy also requires significant infrastructure and is thus not always routinely achievable.

X-ray diffraction (XRD) has the advantage of being a fairly standard laboratory technique which probes the crystalline structure of a statistically large number of NCs in a single run. While XRD patterns are commonly used to identify the phases present in nanocrystalline materials, in conjunction with simulation, XRD may be used to confirm the morphology of NCs determined from electron microscopy. The Debye equation allows for the simulation of XRD patterns based on atomistic models of NCs.[27,58] An atomistic model which is consistent with both XRD and TEM results provides an accurate picture of the average NC morphology in a given sample. We have performed simulations of XRD patterns for three samples using atomistic models derived from a statistical analysis of TEM images in which the dimensions of 200 or more individual NCs are measured. Figure 2 shows the experimental powder XRD patterns together with the simulated spectra. TiO_2 NCs are dissolved in toluene and placed in glass capillaries, and the X-ray diffraction patterns are measured in transmission mode, eliminating the effects of preferred orientation which are commonly observed in films of anisotropic NCs.[70]

Interestingly, all three anatase TiO_2 NC samples exhibit substantial deviations from standard lattice parameters. The shifting of the (200) peak at $2\theta \approx 48.0°$ and (004) peak at $2\theta \approx 37.8°$ clearly indicates expansion in the *a*-axis (0.3%) and compression in the *c*-axis (0.39−0.55%), respectively. Similar results have been reported previously for nanosized anatase TiO_2, but significant changes in the lattice parameters are not typically observed until the dimension of the crystallites is less than 10 nm.[71,72] Changes in the lattice parameters may be caused by the presence of oxygen vacancies or fluorine on the particle surface, as described below. While the origins are beyond the scope of this manuscript, the simultaneous *c*-axis compression and *a*-axis expansion are introduced into the XRD simulation by adjusting the lattice parameters in the atomistic model in order to fit the appropriate peak position.

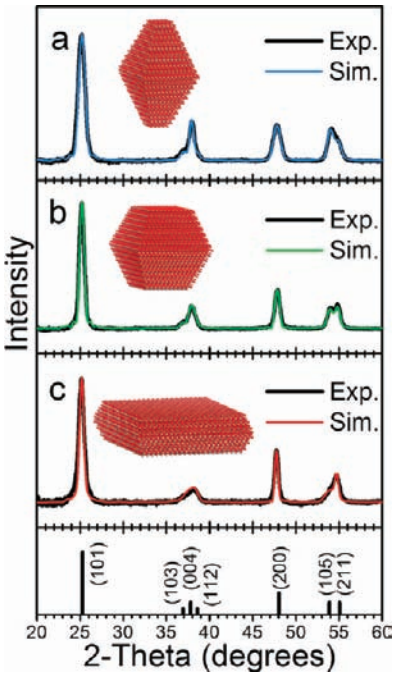

Figure 2. Experimental XRD patterns (thick black lines) plotted with simulation (thin colored lines) for TiO_2 NCs (a) M-OLAM, (b) F-OLAM, and (c) M-ODOL. Insets show atomistic models with accurate percentages of {001} and {101} facets but at a smaller scale (for actual atomistic models, see Figure S4).

Figure 2 shows the experimental and simulated XRD pattern for three samples with different percentages of {001} and {101} facets. Based on the XRD pattern fitting, sample M-OLAM is found to be 18.0 nm in length (along the *c*-axis) and 10.8 nm in width (along the *a*-axis). This is in excellent agreement with results from a statistical analysis of TEM images (Figure S5). Similarly, for the more truncated sample F-OLAM, a length of 10.8 nm and a width of 14.5 nm are determined, while sample M-ODOL, with the highest percentage of {001} facets, is fitted to a 5.8 nm length and 18.2 nm width. Based on the length and width derived from the XRD simulation fitting, we can precisely calculate the percentages of {001} and {101} facets from the atomistic models of NCs through basic geometric calculations (Figure S5). In addition to the three samples measured in transmission mode, XRD patterns for samples Cl-OLAM, Cl-ODOL, and F-ODOL are recorded in reflection mode (Figure S6).

Optical Properties. All of the samples of TiO_2 synthesized in the presence of fluorine were found to be blue in color (Figure 3a). Blue coloration has been reported previously in reduced TiO_2 (TiO_{2-x})[73−77] and in TiO_2 irradiated with UV light under an inert atmosphere[78−80] and is characteristic of free conduction band electrons in TiO_2. In the former case, additional electrons are proposed to result from oxygen vacancies or titanium interstitials which are formed during the synthetic process. In the latter case, band gap illumination produces conduction band electrons which localize on surface Ti atoms, but this coloration is quickly quenched upon exposure to oxygen or other oxidizers,[78,79] except under extremely high photon flux.[80] Figure 3a shows the optical absorption of sample F-OLAM dispersed in CCl_4 from the UV to the IR (300−5500 nm). The spectrum shows a sharp absorption edge at 380 nm (3.2 eV) corresponding to band-to-band transitions, and broad absorption throughout the visible

dx.doi.org/10.1021/ja300823a | J. Am. Chem. Soc. 2012, 134, 6751−6761

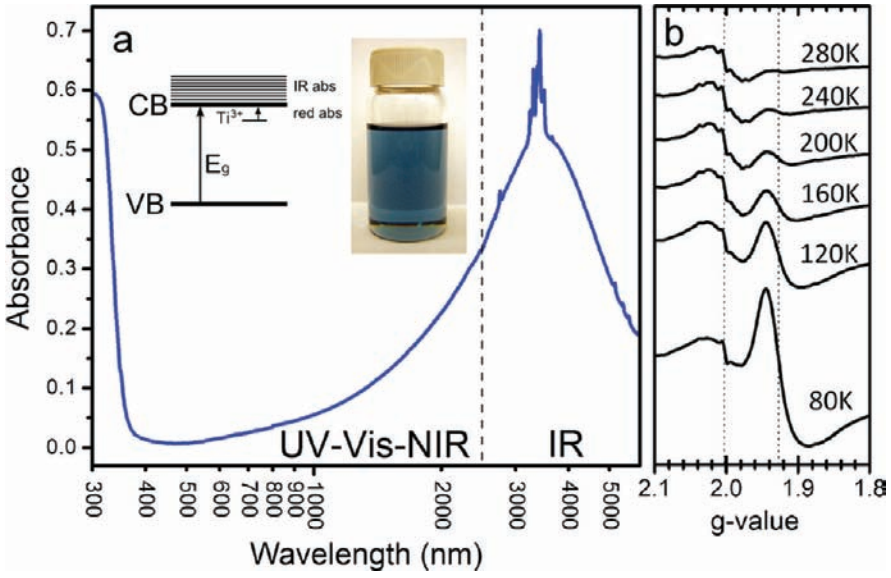

Figure 3. (a) Optical absorption of sample F-OLAM dispersed in CCl_4 (dashed line at 2500 nm indicates where data is joined) and (b) EPR spectra of sample F-OLAM at several temperatures. Inset of (a) shows proposed band diagram of blue TiO_2 NCs and an optical image of TiO_2 NCs dispersed in toluene.

region and NIR, which peaks in the IR at around 3400 nm. The sharp oscillations observed near the peak of absorption and in other regions of the IR (2500−5500 nm) result from the vibrational transitions of surfactant molecules on the particle surface and residual solvent molecules. The diffuse reflectance spectra from 300 to 2500 nm is shown in Figure S7 for all of the synthesized TiO_2 NCs. The absorption at 380 nm is observed in all of the samples, whereas only the NCs synthesized in the presence of fluorine have a broad vis/NIR absorption. The blue coloration is stable in air for months without noticeable changes in the absorbance and persists after annealing under a nitrogen atmosphere at 300 °C. On the other hand, the sample turns white after annealing at 300 °C in air, providing strong evidence for the presence of oxygen vacancies as described above.

We have performed electron paramagnetic resonance (EPR) studies on sample F-OLAM to determine the chemical environment of unpaired electrons in the NCs (Figure 3b). A gradual increase in signal intensity is observed with decreasing temperature at g = 1.927, which has previously been attributed to surface and subsurface paramagnetic Ti^{3+} centers.[78,81,82] This resonance is damped at high temperatures due to fast spin relaxation times.[83] At all temperatures, a broad peak is observed at g = 2.003, which has previously been attributed to electrons localized on oxygen vacancies in TiO_2.[84−86] These results are in agreement with the optical data presented above, strongly suggesting the formation of oxygen vacancies in the synthesized NCs and the presence of free electrons which localize to form Ti^{3+} centers near the NC surface at low temperature. The absence of EPR signals at g = 1.99 and g = 1.96, which are usually observed for Ti^{3+} ions in anatase crystallites, indicates that free electrons do not occupy bulk-like Ti positions in the NCs. A proposed energy level diagram for the blue TiO_2 NCs is shown as an inset in Figure 3a, which depicts band-to-band absorption in the UV, as well as red/NIR and IR absorption which results from the absorption of electrons localized on Ti^{3+} sites and free electrons residing in the conduction band, respectively.

A broad vis−NIR−IR absorption band is commonly attributed to the excitation of conduction band electrons in blue TiO_2 and therefore reflects the density of states of the conduction band.[73,83] On the other hand, the fairly narrow line width of the absorption feature in the IR region (Figure 3a) suggests that the absorption may result from a localized surface plasmon resonance (LSPR). While routinely observed in metallic nanostructures, surface plasmon resonances, which result from the collective oscillation of electrons on the surface of a crystal, have also been recently reported in doped oxides with sufficient free carriers.[87] For highly conductive oxides (indium tin oxide (ITO), aluminum doped zinc oxide (AZO), etc.), the frequency typically lies within the NIR−terahertz (THz) region of the electromagnetic spectrum, depending on dopant concentration.[88] The peak centered at 3400 nm for sample M-OLAM resembles the absorption features of doped oxide NCs recently reported in which an LSPR was identified.[88−90] A plasmonic resonance in TiO_2 should be considered feasible, as oxygen-deficient TiO_2 supports many free carriers and is known to produce highly conductive thin films.[73,91,92]

While the blue coloration and EPR spectra are both readily explained by the presence of oxygen vacancies, an alternative explanation for the Ti^{3+} EPR signal observed in our NCs is the substitutional doping of fluorine into the TiO_2 lattice. In this scenario, each fluorine atom that substitutes for an oxygen atom contributes an electron to the conduction band, similarly producing EPR signatures for Ti^{3+} at low temperature.[93] At first glance, this fluorine doping mechanism appears to be more probable, considering that using $TiCl_4$ (or $TiBr_4$) as the titanium precursor under identical reaction conditions results in TiO_2 NCs without blue coloration, and because no additional reductive gases are expected to form in the presence of TiF_4. On the other hand, the only optical changes observed for fluorine doped TiO_2 in the literature have been minor band gap shifts, with no significant red/NIR absorption.[93−95]

To clarify this issue, the nature of the interaction between fluorine and TiO_2 is further investigated using microanalysis techniques. Fluorine is detectable in sample F-ODOL using

dx.doi.org/10.1021/ja300823a | J. Am. Chem. Soc. 2012, 134, 6751−6761

energy dispersive X-ray spectroscopy (EDS), despite the fact that the technique is rather insensitive to light elements such as fluorine (Figure S8). However, the relatively low concentrations make quantitative analysis using EDS prohibitive. Consequently, X-ray photoelectron spectroscopy (XPS) studies were undertaken, which not only allow for the quantification of the fluorine content but also provide information regarding the chemical environment of fluorine atoms in the NC samples. Figure 4 shows a survey and high resolution F1s XPS spectrum

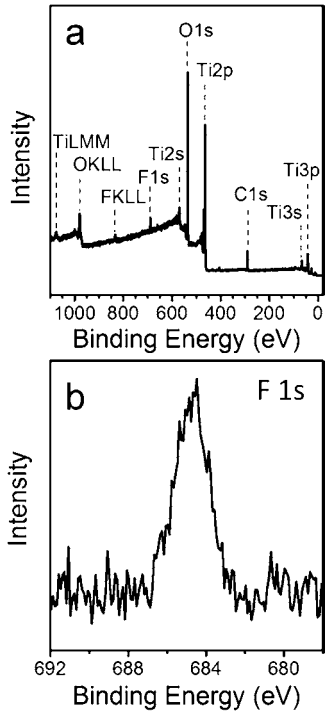

Figure 4. (a) XPS survey spectrum and (b) high resolution XPS spectrum of the F 1s peak for sample F-OLAM.

for sample F-OLAM, while XPS spectra for M-OLAM and F-ODOL are depicted in Figure S9. The centroid of the F1s peak at 684.8 ± 0.2 eV in all samples is consistent with fluorine bound to the surface of TiO_2 and does not indicate the presence of $TiO_{2-x}F_x$ species.[8,20,75,93] Based on this evidence, we propose that while fluorine is not substitutionally doped into the TiO_2 lattice, fluorine species play an important role in the formation of oxygen vacancies under the reported synthetic conditions. It is possible that the very strong bond between Ti and F (the only bond to titanium stronger than Ti−O)[96] facilitates oxygen vacancy formation.

Table S1 shows the total [F]/[Ti] ratio derived from the XPS results for samples M-OLAM, F-OLAM, and F-ODOL. The NC sample with the largest percentage of {001} facets (F-ODOL) also has the highest fluorine content. This is in agreement with previous studies which indicate that fluoride bound to the {001} facet remains even after multiple washing steps and is only removed after annealing at high temperature or treatment with concentrated sodium hydroxide (NaOH).[8,9] Figure S9 and Table S1 also display the HR Ti 2p spectra and the $[Ti^{3+}]/[Ti^{4+}]$ ratios for the three analyzed samples, respectively. These data confirm the presence of Ti^{3+} in the blue TiO_2 NCs and indicate that the $[Ti^{3+}]/[Ti^{4+}]$ ratio lies between 0.014 and 0.033.

Photocatalytic Hydrogen Evolution. The high uniformity of the synthesized samples enables us to determine the influence of the {001} and {101} facets on the photocatalytic activity of oxygen deficient anatase TiO_2 NCs. It must be underlined that the term photocatalysis encompasses a wide variety of reactions performed under different reaction conditions, making this field quite fragmented. In the present work, we investigate the evolution of hydrogen in the presence of methanol as a sacrificial agent under simulated solar light for three samples of oxygen deficient anatase NCs. This model reaction, known also as photoreforming, is gaining increasing interest in view of the sustainable production of hydrogen.[97,98]

The NCs synthesized using our method are highly hydrophobic due to the surfactants bound to the particle surface and are not dispersible in aqueous solutions.[49] Therefore, a recently developed ligand-exchange technique utilizing $NOBF_4$ is used to disperse the photocatalyst in aqueous solution. After this simple procedure, the resulting NCs are dispersible in water and aqueous mixtures, and standard methanol photoreforming tests can then be carried out.[42] This procedure accounts for a further advantage of the present method, which couples the extremely precise morphological control obtained through nonaqueous synthetic techniques with the subsequent water dispersibility after ligand exchange, which could be further exploited for biological applications. After $NOBF_4$ treatment, the water-dispersible NCs are still fluorine terminated on the surface. Recent publications indicate that the presence of surface fluorine results in similar H_2 evolution rates for the {101} and {001} facets of micrometer-sized anatase TiO_2 crystals.[22] In the present work, we remove fluorine from the samples with a published procedure using NaOH treatment and compare the activity before and after the treatment.[19,55]

Figure 5 shows the rate of photocatalytic hydrogen production as a function of time under simulated solar irradiation for three selected samples of Pt/TiO_2 with different percentages of {001} and {101} facets prepared as described above, both fluorinated and NaOH treated (data for all of the fluorinated samples is shown in Figure S10). Platinum is photodeposited on the NCs to obtain a final metal loading of 1 wt % in all the cases. The metal is necessary to ensure that photogenerated electrons are capable of reducing protons to molecular hydrogen.[99,100] No hydrogen is evolved in the absence of Pt or photocatalyst or when samples are illuminated with only visible light ($\lambda > 430$ nm). Very low, more sustainable Pt loadings (0.1 wt %) show similar or even better overall performances (Figure S11), but a 1 wt % Pt loading is necessary to simplify TEM characterization of the materials. An induction period of ∼1 h is observed before the samples reach a maximum and stable H_2 evolution rate as complete photodeposition of Pt occurs. All the samples exhibit good performances, with up to ∼2.1 mmol H_2 h^{-1} g^{-1} evolved under solar illumination. Although this value is lower than that obtained under similar conditions with platinized TiO_2 produced using advanced engineering,[101] it is a remarkable result especially for the fluorinated samples (Figure 5a). In fact, both theoretical and experimental studies suggest that the presence of F on the {001} facet of anatase TiO_2 can result in unfavorable water dissociation[102] and reduced H_2 evolution rates.[103] It must be noted that different mechanisms can be active for methanol photoreforming. In particular, there exists a direct pathway in which methanol adsorbs on the surface and is subsequently oxidized by photogenerated holes and an indirect

dx.doi.org/10.1021/ja300823a | J. Am. Chem. Soc. 2012, 134, 6751−6761

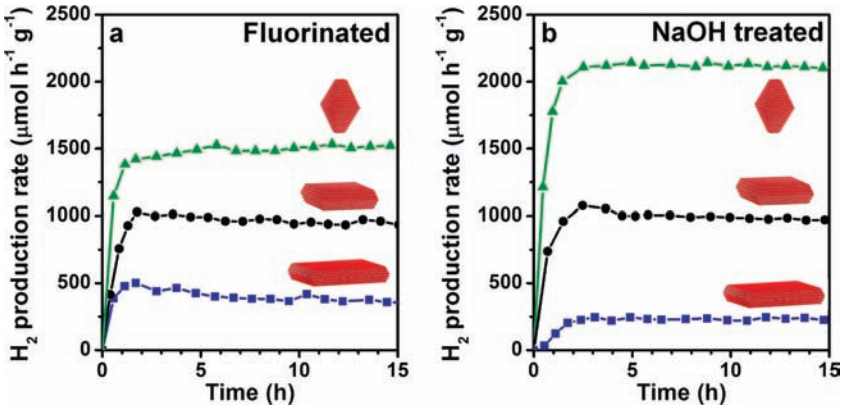

Figure 5. Hydrogen production rate from 1 wt % Pt loaded samples of ligand exchanged, (a) fluorinated and (b) NaOH-treated TiO_2 NCs under solar illumination in 1:1 mixtures of MeOH/H_2O. Samples are M-OLAM (green triangles), M-ODOL (black circles), and F-ODOL (blue squares).

one in which water adsorbs and the hydroxyl radicals that form act as the true oxidative species.[104] In the present work, a high concentration of methanol (50% by volume) is used, which results in the concomitant high production of formaldehyde (determined by GC-MS) and scarcity of CO_2 in the outflow. These observations suggest the predominance of the direct oxidation pathway, in which methanol interacts directly with the surface, truly acting as a hole scavenger, and that very little water oxidation occurs.

We observe that higher percentages of {101} facets correlate with higher photocatalytic activity for both treated and untreated samples, indicating that the {101} is more active for the production of hydrogen from methanolic solutions under the employed experimental conditions. TEM images of the samples indicate minor differences in the Pt size distributions (Figure S12), excluding a major contribution of different Pt dispersions to the reactivity of the various photocatalysts. Our results conflict with studies which indicate that the {001} facet is more reactive than {101} for photocatalytic applications due to having a more open structure with exposed undercoordinated Ti moieties.[16,105,106] On the other hand, it is in line with a recent report which suggests that the {101} surface may, in fact, be more active than the {001} for hydrogen evolution under similar reaction conditions using micrometer-sized anatase cyrstals.[22]

Analysis of the samples before and after the NaOH treatment reveals intriguing changes in photocatalytic activity. The sample F-ODOL, with the largest percentage of exposed {001} facets, shows a *decrease* in photocatalytic activity after NaOH treatment. On the contrary, the sample M-OLAM, with the largest percentage of exposed {101} facets, shows an *increase* of the photocatalytic activity. To complete the picture, the activity of the sample M-ODOL, where the percentages of {101} and {001} facets are almost equal, has very similar activity after treatment. This observation implies that the activity of {101} facets is increased by NaOH treatment and that of {001} is decreased, and that these two effects are near perfectly balanced in the M-ODOL sample, where the two facets coexist equally. Although a definitive explanation for the observed trend is beyond the scope of the present work, it is reasonable to infer that the differences in the activity can be related to both structural and electronic factors. The presence of fluorine may increase the electron and hole lifetimes in the sample F-ODOL, where many undercoordinated Ti moieties are present on the {001} facet, the benefits of which are lost upon fluorine removal.[107] Furthermore, the increased hydroxylation of the surface following the NaOH treatment might saturate the Ti moieties on the {001} facet leading to a loss of the special reactivity demonstrated by the Ti_{5c} centers. Likewise, in the case of the sample M-OLAM with exposed {101} facets, the residual fluorine could hinder the adsorption of methanol on the octahedral Ti_{6c} sites, thus contributing to the relatively low activity when fluorinated. In this case, the removal of fluorine improves adsorption and decomposition of methanol following hydroxylation of the surface.

Table S2 shows the surface area of the three samples for which the photocatalytic activity is measured before and after NaOH treatment. The trend in activity observed cannot be simply related to a difference in specific surface area of the samples. In fact, in the case of porous heterogeneous photocatalysts, the actual operating surface is unknown since portions of the sample are not illuminated as a consequence of internal shading. This element accounts for the intrinsic difficulties in obtaining reliable areal parameters in photocatalysis.[108] Furthermore, routine BET measurements can underestimate the surface area of powders composed of assembled NCs, particularly in the case of the nanoplates synthesized in this work where face-to-face packing can dramatically reduce the accessible surface area. During a photoreforming reaction in which the NCs are in the dispersed state, less association between particles would cause more surface area to be exposed. In addition, when the reaction is performed in liquid phase, mass transfer effects may limit the observed activity. Supporting this argument, we observe that NaOH treatment increases the surface area of the sample F-ODOL by almost three times (Table S2), while the photocatalytic activity drops, excluding a major effect of surface area on the presented trends. In addition, the surface area of the NCs may be accurately estimated using the atomistic models derived from XRD analysis (Figure S5 and Table S2). For sample M-OLAM, the calculated surface area is 136 $m^2\ g^{-1}$ compared to a measured value of 134 $m^2\ g^{-1}$, again indicating the accuracy of the XRD fitting. In contrast, the measured surface area of the two nanoplate samples, M-ODOL and F-ODOL, deviate significantly from the calculated values, demonstrating the effect of nanoplate stacking.

Although further experiments are necessary to understand the observed differences in photocatalytic activity for the production of hydrogen over the {101} and {001} facets of anatase, our experiments utilizing well-defined nanosized TiO_2

crystals suggest that {101} facets are the more photocatalytically active than the {001} facets for the evolution of H_2 by methanol photoreforming in the presence of Pt.

CONCLUSIONS

We have shown that the morphology of TiO_2 NCs 10−100 nm in size may be controlled through a nonaqueous seeded growth method. The precursor TiF_4 enables the exposure of the {001} facet of anatase TiO_2 through the *in situ* release of HF. The fluoride ion from HF binds preferentially to the {001} facet, and the HF concentration is controlled through dilution of TiF_4 with $TiCl_4$ and the choice of cosurfactant, allowing the percentage of {001} and {101} facets to be engineered. XRD experiments, in conjunction with simulation, are introduced as a method to precisely determine the morphology of the produced NCs and quantify the percentage of {001} and {101} facets. In addition to the control provided over the NC shape, particles synthesized in the presence of TiF_4 are found to have blue coloration. The broad vis/NIR absorption is the result of free electrons supplied by oxygen vacancies in the TiO_2 lattice. The photocatalytic activities of three oxygen deficient anatase TiO_2 NC samples after Pt photodeposition indicate that the {101} facet is more active for the production of hydrogen from methanolic solutions under solar illumination.

ASSOCIATED CONTENT

Supporting Information

Representative TEM image of anatase TiO_2 seeds; representative TEM images of particle growth of sample F-OLAM as function of time; actual atomistic models used in X-ray simulations; description of method to determine percentages of {001} and {101} facet and tabulated particle sizes of three NC samples; XRD patterns for samples Cl-OLAM, F-ODOL, and Cl-ODOL; DRS spectra covering the UV−vis−NIR (300−2000 nm); EDS spectrum of sample F-ODOL; high resolution XPS spectra of F 1s and Ti 2p peaks for NC samples; tabulated XPS results; H_2 production rate with different Pt loadings; TEM images of NCs loaded with 1% Pt after 15 h of photoreforming; HRTEM images; textural properties of selected samples before and after NaOH treatment; and instrumental conditions and analysis procedures for XPS data. This material is available free of charge via the Internet at http://pubs.acs.org.

AUTHOR INFORMATION

Corresponding Author

cbmurray@sas.upenn.edu

Notes

The authors declare no competing financial interest.

ACKNOWLEDGMENTS

T.R.G. was supported by the National Science Foundation through the Nano/Bio Interface Center at the University of Pennsylvania Grant Number DMR08-32802. T.-J.P. was supported by the Office of Naval Research, MURI W911NF-08-1-0364. Financial support of the Swiss National Science Foundation (grant to F.M.) is acknowledged. P.F. and M.C. acknowledge the University of Trieste and the Italian Consortium on Materials Science and Technology (INSTM) for the financial support. C.B.M. is grateful for the support of the Richard Perry University Professorship. We thank Douglas Yates for the analytical support at the Penn Regional Nanotechnology Facility.

REFERENCES

(1) U.S. Geological Survey, Mineral commodity summaries 2011: U.S. Geological Survey, 2011, p 172.
(2) Chen, X.; Mao, S. S. *Chem. Rev.* **2007**, *107*, 2891−959.
(3) Fujishima, A.; Zhang, X.; Tryk, D. A. *Surf. Sci. Rep.* **2008**, *63*, 515−582.
(4) Chen, X.; Shen, S.; Guo, L.; Mao, S. S. *Chem. Rev.* **2010**, *110*, 6503−70.
(5) Diebold, U. *Surf. Sci. Rep.* **2003**, *48*, 53−229.
(6) Linsebigler, A. L.; Lu, G.; Yates, J. T., Jr. *Chem. Rev.* **1995**, *95*, 735−758.
(7) Kandiel, T. A.; Feldhoff, A.; Robben, L.; Dillert, R.; Bahnemann, D. W. *Chem. Mater.* **2010**, *22*, 2050−2060.
(8) Yang, H. G.; Sun, C. H.; Qiao, S. Z.; Zou, J.; Liu, G.; Smith, S. C.; Cheng, H. M.; Lu, G. Q. *Nature* **2008**, *453*, 638−41.
(9) Fang, W. Q.; Gong, X.-Q.; Yang, H. G. *J. Phys. Chem. Lett.* **2011**, *2*, 725−734.
(10) Liu, S.; Yu, J.; Jaroniec, M. *Chem. Mater.* **2011**, *23*, 4085−4093.
(11) Liu, G.; Yu, J. C.; Lu, G. Q. M.; Cheng, H.-M. *Chem. Commun.* **2011**, *47*, 6763−83.
(12) Thompson, T. L.; Yates, J. T., Jr. *Chem. Rev.* **2006**, *106*, 4428−53.
(13) Henderson, M. A. *Surf. Sci. Rep.* **2011**, *66*, 185−297.
(14) Lazzeri, M.; Vittadini, A.; Selloni, A. *Phys. Rev. B* **2001**, *63*, 1−9.
(15) Vittadini, A.; Selloni, A.; Rotzinger, F. P.; Grätzel, M. *Phys. Rev. Lett.* **1998**, *81*, 2954−2957.
(16) Gong, X. Q.; Selloni, A. *J. Phys. Chem. B* **2005**, *109*, 19560−19562.
(17) Yang, H. G.; Liu, G.; Qiao, S. Z.; Sun, C. H.; Jin, Y. G.; Smith, S. C.; Zou, J.; Cheng, H. M.; Lu, G. Q. M. *J. Am. Chem. Soc.* **2009**, *131*, 4078−83.
(18) Wu, B.; Guo, C.; Zheng, N.; Xie, Z.; Stucky, G. D. *J. Am. Chem. Soc.* **2008**, *130*, 17563−7.
(19) Han, X.; Kuang, Q.; Jin, M.; Xie, Z.; Zheng, L. *J. Am. Chem. Soc.* **2009**, *131*, 3152−3153.
(20) Liu, G.; Yang, H. G.; Wang, X.; Cheng, L.; Pan, J.; Lu, G. Q. M.; Cheng, H.-M. *J. Am. Chem. Soc.* **2009**, *131*, 12868−9.
(21) Dai, Y.; Cobley, C. M.; Zeng, J.; Sun, Y.; Xia, Y. *Nano Lett.* **2009**, *9*, 2455−9.
(22) Pan, J.; Liu, G.; Lu, G. Q. M.; Cheng, H.-M. *Angew. Chem., Int. Ed.* **2011**, *50*, 2133−7.
(23) Jiang, H. B.; Cuan, Q.; Wen, C. Z.; Xing, J.; Wu, D.; Gong, X.-Q.; Li, C.; Yang, H. G. *Angew. Chem., Int. Ed.* **2011**, *50*, 3764−3768.
(24) Tachikawa, T.; Yamashita, S.; Majima, T. *J. Am. Chem. Soc.* **2011**, *133*, 7197−204.
(25) D'Arienzo, M.; Carbajo, J.; Bahamonde, A.; Crippa, M.; Polizzi, S.; Scotti, R.; Wahba, L.; Morazzoni, F. *J. Am. Chem. Soc.* **2011**, *133*, 17652−61.
(26) Wu, X.; Chen, Z.; Lu, G. Q. M.; Wang, L. *Adv. Funct. Mater.* **2011**, *21*, 4167−4172.
(27) Murray, C. B.; Kagan, C. R.; Bawendi, M. G. *Annu. Rev. Mater. Sci.* **2000**, *30*, 545−610.
(28) Murray, C. B.; Sun, S.; Doyle, H.; Betley, T. *MRS Bull.* **2001**, 985−991.
(29) Park, J.; An, K.; Hwang, Y.; Park, J.-G.; Noh, H.-J.; Kim, J.-Y.; Park, J.-H.; Hwang, N.-M.; Hyeon, T. *Nat. Mater.* **2004**, *3*, 891−5.
(30) Jun, Y.-w.; Choi, J.-s.; Cheon, J. *Angew. Chem., Int. Ed.* **2006**, *45*, 3414−39.
(31) Park, J.; Joo, J.; Kwon, S. G.; Jang, Y.; Hyeon, T. *Angew. Chem., Int. Ed.* **2007**, *46*, 4630−4660.
(32) Ahmadi, T. S.; Wang, Z. L.; Green, T. C.; Henglein, A.; El-Sayed, M. A. *Science* **1996**, *272*, 1924−6.
(33) Burda, C.; Chen, X.; Narayanan, R.; El-Sayed, M. A. *Chem. Rev.* **2005**, *105*, 1025−102.
(34) Bratlie, K. M.; Lee, H.; Komvopoulos, K.; Yang, P.; Somorjai, G. A. *Nano Lett.* **2007**, *7*, 3097−101.

(35) Lee, I.; Delbecq, F.; Morales, R.; Albiter, M. A.; Zaera, F. *Nat. Mater.* **2009**, *8*, 132−8.
(36) Xia, Y.; Xiong, Y.; Lim, B.; Skrabalak, S. E. *Angew. Chem., Int. Ed.* **2009**, *48*, 60−103.
(37) Yamada, Y.; Tsung, C.-K.; Huang, W.; Huo, Z.; Habas, S. E.; Soejima, T.; Aliaga, C. E.; Somorjai, G. A.; Yang, P. *Nat. Chem.* **2011**, *3*, 372−376.
(38) Kang, Y.; Ye, X.; Murray, C. B. *Angew. Chem., Int. Ed.* **2010**, *49*, 6156−9.
(39) Kang, Y.; Murray, C. B. *J. Am. Chem. Soc.* **2010**, *132*, 7568−9.
(40) Joo, J.; Kwon, S. G.; Yu, T.; Cho, M.; Lee, J.; Yoon, J.; Hyeon, T. *J. Phys. Chem. B* **2005**, *109*, 15297−302.
(41) Comparelli, R.; Fanizza, E.; Curri, M. L.; Cozzoli, P. D.; Mascolo, G.; Passino, R.; Agostiano, A. *Appl. Catal., B* **2005**, *55*, 81−91.
(42) Dong, A.; Ye, X.; Chen, J.; Kang, Y.; Gordon, T.; Kikkawa, J. M.; Murray, C. B. *J. Am. Chem. Soc.* **2011**, *133*, 998−1006.
(43) Kuipers, E. W.; Laszlo, C.; Wieldraaijer, W. *Catal. Lett.* **1993**, *17*, 71−79.
(44) Trentler, T. J.; Denler, T. E.; Bertone, J. F.; Agrawal, A.; Colvin, V. L. *J. Am. Chem. Soc.* **1999**, *121*, 1613−1614.
(45) O'Brien, S.; Brus, L.; Murray, C. B. *J. Am. Chem. Soc.* **2001**, *123*, 12085−12086.
(46) Jun, Y.-W.; Casula, M. F.; Sim, J.-H.; Kim, S. Y.; Cheon, J.; Alivisatos, A. P. *J. Am. Chem. Soc.* **2003**, *125*, 15981−5.
(47) Zhang, Z.; Zhong, X.; Liu, S.; Li, D.; Han, M. *Angew. Chem., Int. Ed.* **2005**, *44*, 3466−70.
(48) Koo, B.; Park, J.; Kim, Y.; Choi, S.-H.; Sung, Y.-E.; Hyeon, T. *J. Phys. Chem. B* **2006**, *110*, 24318−23.
(49) Buonsanti, R.; Grillo, V.; Carlino, E.; Giannini, C.; Kipp, T.; Cingolani, R.; Cozzoli, P. D. *J. Am. Chem. Soc.* **2008**, *130*, 11223−33.
(50) Dinh, C.-T.; Nguyen, T.-D.; Kleitz, F.; Do, T.-O. *ACS Nano* **2009**, *3*, 3737−43.
(51) Chen, C.; Hu, R.; Mai, K.; Ren, Z.; Wang, H.; Qian, G.; Wang, Z. *Cryst. Growth Des.* **2011**, *11*, 5221−5226.
(52) Buonsanti, R.; Carlino, E.; Giannini, C.; Altamura, D.; De Marco, L.; Giannuzzi, R.; Manca, M.; Gigli, G.; Cozzoli, P. D. *J. Am. Chem. Soc.* **2011**, *133*, 19216−39.
(53) Yu, H.; Gibbons, P. C.; Kelton, K. F.; Buhro, W. E. *J. Am. Chem. Soc.* **2001**, *123*, 9198−9199.
(54) Jana, N. R.; Gearheart, L.; Murphy, C. J. *Chem. Mater.* **2001**, *13*, 2313−2322.
(55) Minella, M.; Faga, M. G.; Maurino, V.; Minero, C.; Pelizzetti, E.; Coluccia, S.; Martra, G. *Langmuir* **2010**, *26*, 2521−7.
(56) Brown, P. J.; Fox, A. G.; Maslen, E. N.; O'Keefe, M. A.; Willis, B. T. M. *International Tables for Crystallography*; John Wiley & Sons, Ltd.: 2006; Vol. *C*.
(57) Hovestreydt, E. *Acta Crystallogr. A* **1983**, *39*, 268−269.
(58) Hall, B. D.; Monot, R. *Comput. Phys.* **1991**, *5*, 414−414.
(59) Alcock, N. W.; Brown, D. A.; Illson, T. F.; Roe, S. M.; Wallbridge, M. G. H. *J. Chem. Soc., Dalton Trans.* **1991**, 873−873.
(60) Barrow, H.; Brown, D. A.; Alcock, N. W.; Clase, H. J.; Wallbridge, M. G. H. *J. Chem. Soc., Dalton Trans.* **1994**, *1*, 195−195.
(61) Gindl, J.; Liu, F.-Q.; Noltemeyer, M.; Schmidt, H.-G.; Roesky, H. W. *Inorg. Chem.* **1995**, *34*, 5711−5714.
(62) Vioux, A. *Chem. Mater.* **1997**, *9*, 2292−2299.
(63) Niederberger, M.; Bartl, M. H.; Stucky, G. D. *Chem. Mater.* **2002**, *14*, 4364−4370.
(64) Niederberger, M. *Acc. Chem. Res.* **2007**, *40*, 793−800.
(65) Niederberger, M.; Garnweitner, G.; Ba, J.; Polleux, J.; Pinna, N. *Int. J. Nanotechnol.* **2007**, *4*, 263−263.
(66) Chen, Y.; Kim, M.; Lian, G.; Johnson, M. B.; Peng, X. *J. Am. Chem. Soc.* **2005**, *127*, 13331−7.
(67) Padmanabhan, S. C.; Pillai, S. C.; Colreavy, J.; Balakrishnan, S.; McCormack, D. E.; Perova, T. S.; Hinder, S. J.; Kelly, J. M. *Chem. Mater.* **2007**, *19*, 4474−4481.
(68) Lv, Y.; Yu, L.; Huang, H.; Liu, H.; Feng, Y. *Appl. Surf. Sci.* **2009**, *255*, 9548−9552.
(69) Selloni, A. *Nat. Mater.* **2008**, *7*, 613−5.
(70) Paik, T.; Ko, D.-K.; Gordon, T. R.; Doan-Nguyen, V.; Murray, C. B. *ACS Nano* **2011**, *5*, 8322−30.
(71) Swamy, V.; Menzies, D.; Muddle, B. C.; Kuznetsov, A.; Dubrovinsky, L. S.; Dai, Q.; Dmitriev, V. *Appl. Phys. Lett.* **2006**, *88*, 243103−243103.
(72) Ahmad, M. I.; Bhattacharya, S. S. *Appl. Phys. Lett.* **2009**, *95*, 191906−191906.
(73) Khomenko, V. M.; Langer, K.; Rager, H.; Fett, A. *Phys. Chem. Miner.* **1998**, *25*, 338−346.
(74) Liu, H.; Ma, H. T.; Li, X. Z.; Li, W. Z.; Wu, M.; Bao, X. H. *Chemosphere* **2003**, *50*, 39−46.
(75) Liu, G.; Yang, H. G.; Wang, X.; Cheng, L.; Lu, H.; Wang, L.; Lu, G. Q.; Cheng, H.-m. *J. Phys. Chem. C* **2009**, *113*, 21784−21788.
(76) Teleki, A.; Pratsinis, S. E. *Phys. Chem. Chem. Phys.* **2009**, *11*, 3742.
(77) Zuo, F.; Wang, L.; Wu, T.; Zhang, Z.; Borchardt, D.; Feng, P. *J. Am. Chem. Soc.* **2010**, *132*, 11856−7.
(78) Howe, R. F.; Grätzel, M. *J. Phys. Chem.* **1985**, *89*, 4495−4499.
(79) Howe, R. F.; Grätzel, M. *J. Phys. Chem.* **1987**, *91*, 3906−3909.
(80) Torimoto, T.; Fox, R. J.; Fox, M. A. *J. Electrochem. Soc.* **1996**, *143*, 3712−3717.
(81) Rajh, T.; Ostafin, A. E.; Micic, O. I.; Tiede, D. M.; Thurnauer, M. C. *J. Phys. Chem.* **1996**, *100*, 4538−4545.
(82) Livraghi, S.; Chiesa, M.; Paganini, M. C.; Giamello, E. *J. Phys. Chem. C* **2011**, *115*, 25413−25421.
(83) Berger, T.; Sterrer, M.; Diwald, O.; Knözinger, E.; Panayotov, D.; Thompson, T. L.; Yates, J. T., Jr. *J. Phys. Chem. B* **2005**, *109*, 6061−8.
(84) Prokes, S. M.; Gole, J. L.; Chen, X.; Burda, C.; Carlos, W. E. *Adv. Funct. Mater.* **2005**, *15*, 161−167.
(85) Zhang, S.; Li, W.; Jin, Z.; Yang, J.; Zhang, J.; Du, Z.; Zhang, Z. *J. Solid State Chem.* **2004**, *177*, 1365−1371.
(86) Li, L.; Li, G.; Xu, J.; Zheng, J.; Tong, W.; Hu, W. *Phys. Chem. Chem. Phys.* **2010**, 10857−10864.
(87) Rhodes, C.; Franzen, S.; Maria, J.-P.; Losego, M.; Leonard, D. N.; Laughlin, B.; Duscher, G.; Weibel, S. *J. Appl. Phys.* **2006**, *100*, 054905−054905.
(88) Kanehara, M.; Koike, H.; Yoshinaga, T.; Teranishi, T. *J. Am. Chem. Soc.* **2009**, *131*, 17736−7.
(89) Buonsanti, R.; Llordes, A.; Aloni, S.; Helms, B. A.; Milliron, D. J. *Nano Lett.* **2011**, *11*, 4706−4710.
(90) Manthiram, K.; Alivisatos, A. P. *J. Am. Chem. Soc.* **2012**, *134*, 3995−3998.
(91) Khader, M. M.; Kheiri, F. M. N.; El-Anadouli, B. E.; Ateya, B. G. *J. Phys. Chem.* **1993**, *97*, 6074−6077.
(92) Seo, H.; Baker, L. R.; Hervier, A.; Kim, J.; Whitten, J. L.; Somorjai, G. A. *Nano Lett.* **2011**, *11*, 751−6.
(93) Czoska, A. M.; Livraghi, S.; Chiesa, M.; Giamello, E.; Agnoli, S.; Granozzi, G.; Finazzi, E.; Valentin, C. D.; Pacchioni, G. *J. Phys. Chem. C* **2008**, *112*, 8951−8956.
(94) Yu, J. C.; Yu, J.; Ho, W.; Jiang, Z.; Zhang, L. *Chem. Mater.* **2002**, *14*, 3808−3816.
(95) Todorova, N.; Giannakopoulou, T.; Vaimakis, T.; Trapalis, C. *Mater. Sci. Eng., B* **2008**, *152*, 50−54.
(96) Moss, J. H.; Parfitt, G. D.; Fright, A. *Colloid Polym. Sci.* **1978**, *256*, 1121−1130.
(97) Cargnello, M.; Gasparotto, A.; Gombac, V.; Montini, T.; Barreca, D.; Fornasiero, P. *Eur. J. Inorg. Chem.* **2011**, *2011*, 4309−4323.
(98) Kondarides, D. I.; Daskalaki, V. M.; Patsoura, A.; Verykios, X. E. *Catal. Lett.* **2007**, *122*, 26−32.
(99) Osterloh, F. E. *Chem. Mater.* **2008**, *20*, 35−54.
(100) Barreca, D.; Carraro, G.; Gombac, V.; Gasparotto, A.; Maccato, C.; Fornasiero, P.; Tondello, E. *Adv. Funct. Mater.* **2011**, *21*, 2611−2623.
(101) Chen, X.; Liu, L.; Yu, P. Y.; Mao, S. S. *Science* **2011**, *746*, 746−50.
(102) Sun, C.; Selloni, A.; Du, A.; Smith, S. C. *J. Phys. Chem. C* **2011**, *115*, 17092−17096.

(103) Liu, G.; Sun, C.; Yang, H. G.; Smith, S. C.; Wang, L.; Lu, G. Q. M.; Cheng, H.-M. *Chem. Commun.* **2010**, *46*, 755−757.
(104) Chiarello, G. L.; Ferri, D.; Selli, E. *J. Catal.* **2011**, *280*, 168−177.
(105) Amano, F.; Prieto-Mahaney, O.-O.; Terada, Y.; Yasumoto, T.; Shibayama, T.; Ohtani, B. *Chem. Mater.* **2009**, *21*, 2601−2603.
(106) Yu, J.; Qi, L.; Jaroniec, M. *J. Phys. Chem. C* **2010**, *114*, 13118−13125.
(107) Montoya, J. F.; Salvador, P. *Appl. Catal., B* **2010**, *94*, 97−107.
(108) Braslavsky, S. E.; Braun, A. M.; Cassano, A. E.; Emeline, A. V.; Litter, M. I.; Palmisano, L.; Parmon, V. N.; Serpone, N. *Pure Appl. Chem.* **2011**, *83*, 931−1014.